Supplementary Material: Nonlinear Stage of Modulational Instability in Repulsive Two-Component Bose-Einstein Condensates

I. EXPERIMENTAL SETUP

Our experiments begin with a combination of laser cooling and evaporative cooling resulting in a Bose-Einstein condensate (BEC) composed of ^{87}Rb atoms prepared in the $|F, m_F\rangle = |1, -1\rangle$ hyperfine state. The atoms are supported against gravity in an optical dipole trap formed by a single, tightly focused laser beam with a wavelength of 1064 nm that propagates horizontally. This optical trap is state independent, simultaneously trapping different hyperfine states in an elongated harmonic potential with trap frequencies of $(\omega_x, \omega_y, \omega_z) = 2\pi \times (2.5, 246, 261)$ Hz.

To generate a repulsive barrier at the center of the cloud, a second beam with wavelength 660 nm is turned on in the vertical direction, splitting the BEC into two halves along its elongated axis. Similarly to the attractive dipole trap beam, this wavelength is sufficiently detuned from atomic resonances to produce a state-independent potential, and in particular blue detuned resulting in a repulsive barrier. Next, a homogeneous magnetic bias field of 10 G is applied that separates the energy levels of the hyperfine states, allowing us to later prepare arbitrary mixtures of states by driving radio frequency (RF) transitions (within the $F = 1$ manifold or the $F = 2$ manifold) or microwave (MW) transitions (between the $F = 1$ and $F = 2$ manifolds). The BEC is allowed to equilibrate in the presence of the magnetic field and the repulsive barrier for 2 seconds, before proceeding with the state preparations. At this point, the BEC contains approximately 9×10^5 atoms.

To prepare a 50:50 population mixture of atoms in the $|1, 0\rangle$ and $|2, 0\rangle$ states, we first apply a 51 μs RF pulse on the $|1, -1\rangle$ to $|1, 0\rangle$ transition to transfer 50% of the atoms from the $|1, -1\rangle$ state to the $|1, 0\rangle$ state. This is followed by a 2 ms MW frequency sweep across the $|1, -1\rangle$ to $|2, 0\rangle$ transition to transfer all remaining $|1, -1\rangle$ atoms to the $|2, 0\rangle$ state using an adiabatic rapid passage. The preparation of the state mixture forms the starting point for the evolution described in the main text. During this evolution, both components remain trapped in the optical confinement described above.

During the evolution, some loss of population occurs in the $F = 2$ spin manifold due to spin-changing collisions. Fig. S1 shows the experimentally observed population fraction of each spin state for the data used in Fig. 1 of the main text, normalized to the initial 50:50 populations. The atom loss rate is phenomenologically captured by an exponential fit with decay time of approximately $\tau = 220$ ms and then incorporated into the numerical simulations as a time dependent loss rate in the $F = 2$ population.

To image the atomic cloud, we first transfer all atoms that are in the $|2, 0\rangle$ state back into the $|1, -1\rangle$ state using again a 2 ms MW sweep. The optical trap is removed and a Stern-Gerlach procedure is employed to separate the two hyperfine states vertically as they fall, allowing the two spin populations to be imaged at separate regions of the CCD camera. This procedure relies on the fact that atoms in the $|1, -1\rangle$ or $|1, 0\rangle$ state have different magnetic moments. Therefore, a brief application of a vertical magnetic gradient leads to a differential force on the two states so that they separate vertically in a short time-of-flight period. Images are then acquired using a 10 μs long illumination pulse on the $F = 1$ to $F' = 1$ transition. This imaging procedure is destructive, requiring repeated runs of the experiment to produce a time sequence. The spontaneous MI observed at longer times is irreproducible, however, the barrier induced dynamics is highly reproducible and thus the time evolution can fully be studied even using a succession of experimental runs with destructive imaging.

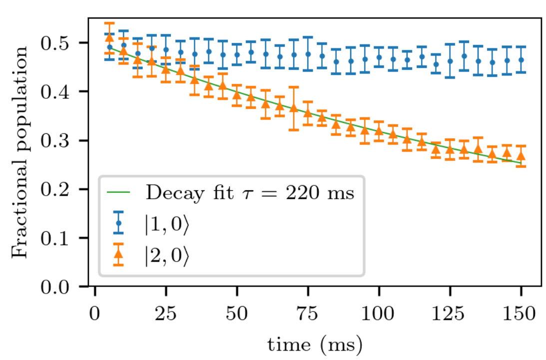

FIG. S1. Fractional populations of the two spin populations over time corresponding to the data shown in Fig. 1 of the main text. An exponential fit to the decay in the $|2, 0\rangle$ population is shown to have a time constant of $\tau = 220$ ms.

II. ONE-DIMENSIONAL REDUCTION

We begin by illustrating the correspondence between the three-dimensional (3D) Gross-Pitaevskii equation (GPE),

$$i\hbar\frac{\partial\Psi}{\partial t}=\left[-\frac{\hbar^2}{2M}\nabla_{\mathbf{r}}^2+V(\mathbf{r})+g^{(3\mathrm{D})}|\Psi|^2\right]\Psi\,, \tag{S1}$$

and the one-dimensional (1D) nonlinear Schrödinger (NLS) equation,

$$iq_t+q_{xx}-2g|q|^2q=0\,. \tag{S2}$$

For simplicity, we focus on the single component case, but the following discussion can be easily extended to multicomponent systems.

In order to achieve effective 1D dynamics, it is important to avoid excitations in the transverse directions. This can be accomplished by employing a tight transverse cigar-shaped trapping potential, i.e., $\omega_x \ll \omega_\perp$, with $a_\perp < \xi$, or equivalently $\hbar\omega_\perp > \mu$. Here, $a_\perp = \sqrt{\hbar/M\omega_\perp}$ is the transverse harmonic oscillator length, ξ denotes the healing length of the Bose gas, and μ is the chemical potential. Thus, the 3D wavefuntion, $\Psi(\mathbf{r},t)$, can be decomposed into longitudinal, $\psi(x,t)$, and transverse, $\chi(y,z)$, degrees-of-freedom, namely $\Psi(\mathbf{r},t)=\psi(x,t)\chi(y,z)e^{-i\mu t/\hbar}$. Subsequently, integrating out the transverse degrees-of-freedom [1], we obtain the 1D GPE,

$$i\hbar\frac{\partial\psi}{\partial t}=\left[-\frac{\hbar^2}{2M}\frac{\partial^2}{\partial x^2}+V(x)+g^{(1\mathrm{D})}|\psi|^2\right]\psi\,, \tag{S3}$$

where $V(x)=M\omega_x x^2/2$ and $g^{(1D)}$ denotes an effective 1D interaction strength. Lastly, with the change of variables $x\to a_\perp x'$, $t\to\omega_\perp^{-1}t'$, and $\psi\to a_\perp^{-1/2}\psi'$, Eq. (S3) becomes nondimensional,

$$i\frac{\partial\psi'}{\partial t'}=\left[-\frac{1}{2}\frac{\partial^2}{\partial x'^2}+V'(x')+g'|\psi'|^2\right]\psi'\,, \tag{S4}$$

with $V'(x')=V(x')a_\perp^2/\hbar\omega_\perp$, and $g'=g^{(1D)}/\hbar\omega_\perp a_\perp$. Apparently, if $V'(x')=0$ and $t'\to t'/2$, we recover the NLS Eq. (S2).

Here, we would also like to emphasize that, typically, an expression for $g^{(1\mathrm{D})}$ is obtained when integrating out the transverse degrees-of-freedom. In order to do so, one needs to solve an auxiliary problem under suitable assumptions. For instance, Eq. (S3) can be obtained by assuming that the solution of the transverse degrees-of-freedom corresponds (in a suitably dilute limit) to a Gaussian profile [2]. If instead it is assumed that they correspond to a Thomas-Fermi profile, one obtains a different model derived in [3]. Here, despite achieving effective 1D dynamics, the transverse degrees-of-freedom do not totally match either of the aforementioned assumptions, and thus we opted to identify the effective $g^{(1\mathrm{D})}$ using a more empirical approach to match the experiment, keeping in mind the fact that $\int|\Psi(\mathbf{r},t)|^2\mathrm{d}\mathbf{r}=1$, and subsequently $\int|\chi(y,z,t)|^2\mathrm{d}y\,\mathrm{d}z=1$ and $\int|\psi(x,t)|^2\mathrm{d}x=1$. More specifically, one can solve the time-independent 1D GPE for a chosen $g^{(1\mathrm{D})}$ under the constraint that both the numerical and experimental radius of the BEC must coincide. However, if $g^{(1\mathrm{D})}$ has not been obtained through the above reduction, the last of the three aforementioned equalities will not be automatically fulfilled. Hence, we identify η such that $\int|\psi(x,t)|^2\mathrm{d}x=\eta$ instead. Here, we interpret η as a corrective coefficient to the assumptions taken to solve the auxiliary problem. Then, by inferring on the form of the interaction term in Eq. (S3), we can redefine $g^{(1\mathrm{D})}\to g^{(1\mathrm{D})}_{\mathrm{eff}}=\eta g^{(1\mathrm{D})}$, so that $\int|\psi(x,t)|^2\mathrm{d}x=1$.

III. LINEARIZED STABILITY ANALYSIS OF THE COUPLED NLS SYSTEM

Below, we present the linearized stability analysis for the background solution of a general coupled system of NLS equations for the field $\mathbf{q}(x,t)=(q_1(x,t),q_2(x,t))^T$, which read

$$iq_{1,t}+q_{1,xx}-2(g_{11}|q_1|^2+g_{12}|q_2|^2)\,q_1=0\,, \tag{S5a}$$
$$iq_{2,t}+q_{2,xx}-2(g_{21}|q_1|^2+g_{22}|q_2|^2)\,q_2=0\,. \tag{S5b}$$

The relevant analysis has been provided earlier (see, as a relevant example, [4, 5]), yet we include it here for reasons of completeness.

This system of equations admits the uniform background solution $\mathbf{q}_o(x,t)=(Q_1\,e^{i\mu_1 t},Q_2\,e^{i\mu_2 t})$, with Q_1 and Q_2 being arbitrary real constants (which can be taken to be non-negative thanks to the phase invariance of the coupled NLS system (S5) without loss of generality). Accordingly, from the stationary equations of motion we obtain the chemical potentials of each component

$\mu_i = 2(g_{ii}Q_i^2 + g_{ij}Q_j^2)$ with $i \neq j = 1,2$. It is convenient to perform a trivial phase rotation and consider the modified field $\mathbf{q}(x,t) = (q_1(x,t), q_2(x,t))^T$ with $\tilde{q}_j(x,t) = q_j(x,t)\,e^{-i\mu_j t}$, $j = 1,2$, which satisfies the NLS equations

$$i\,\tilde{q}_{1,t} + \tilde{q}_{1,xx} - 2(g_{11}|\tilde{q}_1|^2 + g_{12}|\tilde{q}_2|^2 - \mu_1)\,\tilde{q}_1 = 0\,, \tag{S6a}$$

$$i\,\tilde{q}_{2,t} + \tilde{q}_{2,xx} - 2(g_{21}|\tilde{q}_1|^2 + g_{22}|\tilde{q}_2|^2 - \mu_2)\,\tilde{q}_2 = 0\,. \tag{S6b}$$

It is evident that these admit the constant solution $\mathbf{q}_o(x,t) = (Q_1, Q_2)$. The reason for considering a system with uniform background and no potential is twofold: (i) this is the simplest setting that gives rise to the phenomena in question (MI-induced DSW); (ii) the results of the analysis with no potential and a uniform background are also applicable to the case of a sharp spatial transition between zero and non-zero density background (e.g., see Ref. [6]).

Next, we search for solutions representing a small perturbation of the constant background, namely $\tilde{q}_j(x,t) = Q_j(1 + w_j(x,t))$ with $|w_j(x,t)| \ll 1$, $j = 1,2$. Substituting this ansatz into Eqs. (S6) and neglecting quadratic and higher-order terms we arrive to the linearized coupled NLS system

$$i\,w_{1,t} + w_{1,xx} - 2Q_1^2 g_{11}(w_1 + w_1^*) - 2Q_2^2 g_{12}(w_2 + w_2^*) = 0, \tag{S7a}$$

$$i\,w_{2,t} + w_{2,xx} - 2Q_1^2 g_{21}(w_1 + w_1^*) - 2Q_2^2 g_{22}(w_2 + w_2^*) = 0\,, \tag{S7b}$$

where the asterisk denotes complex conjugation. Subsequently, it is possible to rewrite the above system into four individual evolution equations for the real and the imaginary components, by letting $w_j(x,t) = u_j(x,t) + i\,v_j(x,t)$ with $u_j(x,t)$ and $v_j(x,t)$ being real-valued, for $j = 1,2$. As such, we obtain the following system

$$u_{1,t} + v_{1,xx} = 0, \tag{S8a}$$

$$u_{2,t} + v_{2,xx} = 0, \tag{S8b}$$

$$v_{1,t} - u_{1,xx} + 4Q_1^2 g_{11}u_1 + 4Q_2^2 g_{12}u_2 = 0, \tag{S8c}$$

$$v_{2,t} - u_{2,xx} + 4Q_1^2 g_{21}u_1 + 4Q_2^2 g_{22}u_2 = 0. \tag{S8d}$$

Assuming plane-wave solutions of the above system in the form $(u_j(x,t), v_j(x,t)) = (U_j, V_j)\,e^{i(kx-\omega t)}$, $j = 1,2$, we can derive the linear homogeneous system of equations $M\mathbf{U} = 0$, where $\mathbf{U} = (U_1, U_2, V_1, V_2)^T$ and the coefficient matrix M reads

$$M = \begin{pmatrix} k^2 + 4g_{11}Q_1^2 & 4g_{21}Q_1^2 & i\omega & 0 \\ 4g_{12}Q_2^2 & k^2 + 4g_{22}Q_2^2 & 0 & i\omega \\ -i\omega & 0 & k^2 & 0 \\ 0 & -i\omega & 0 & k^2 \end{pmatrix}. \tag{S9}$$

Apparently, nontrivial solutions are obtained when $\det(M) = 0$. This yields two different branches for the linearized dispersion relation

$$\omega_\pm^2 = k^2\Big(k^2 + 2(g_{11}Q_1^2 + g_{22}Q_2^2) \pm 2\sqrt{\Delta}\Big), \tag{S10a}$$

where the interaction and amplitude dependent parameter

$$\Delta = g_{11}^2 Q_1^4 + g_{22}^2 Q_2^4 + 2Q_1^2 Q_2^2\left(2g_{12}g_{21} - g_{11}g_{22}\right). \tag{S10b}$$

It is worthwhile to mention that this dispersion relation holds for arbitrary particle and mass imbalanced repulsive two-component Bose gases.

IV. SPEED OF SOUND AND MI CONDITION

The solution branch obtained from ω_+^2 given by Eq. (S10a) yields sound waves in the limit $k \to 0$. Indeed, it is straightforward to verify that, for this branch, the linearized group velocity associated with the branch $\omega_+(k)$ of the dispersion relation, $c_g(k) = d\omega_+/dk$, at $k = 0$ takes the form

$$c_g(0) = \sqrt{2}\sqrt{g_{11}Q_1^2 + g_{22}Q_2^2 + \sqrt{\Delta}}. \tag{S11}$$

In the limiting (integrable) case where $g_{i,j} = 1$ and the amplitudes Q_1 and Q_2 are normalized so that $Q_1^2 + Q_2^2 = 1$, one simply obtains $c_g(0) = 2$.

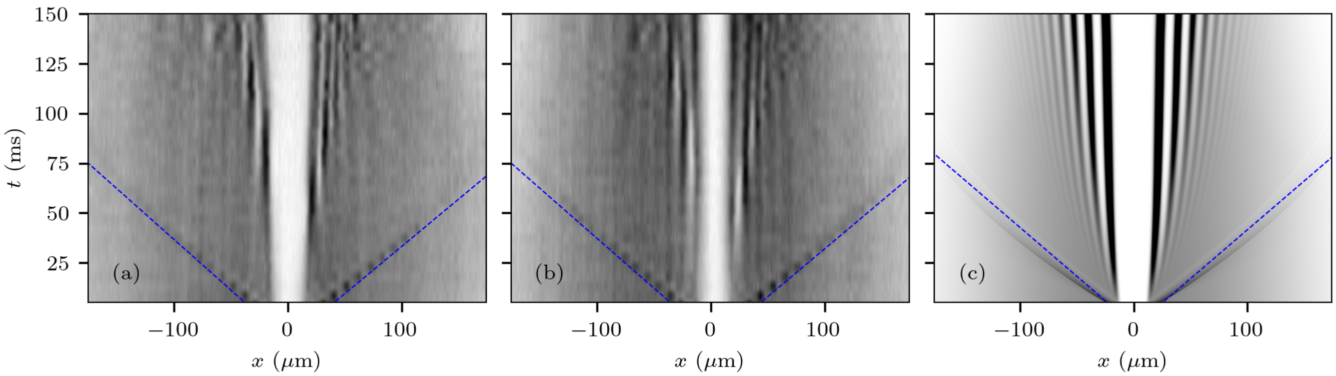

FIG. S2. Experimental and numerical determination of the speed of sound. An equal spin mixture of (a) $|2,0\rangle$ and (b) $|1,0\rangle$ is prepared in the presence of an optical barrier. A sudden increase of the barrier height is used to induce sound waves. Each panel is an average over 10 experimental realizations for every 5 ms. Blue lines mark the linear fit to the traveling sound pulses from the experiment used to determine the speed of sound, averaging at $v_s = 2.0(1)$ μm/ms. (c) 1D GPE simulations of the experimental procedure showing a consistent result for the speed of sound compared to the average over the experimental results, shown as blue lines.

This branch corresponds to the normal speed of sound in the fluid. As a consistency check, we determine this speed of sound in the context of the 1D GPE simulations as well as in the experiment. In both cases, we prepare an equally populated spin mixture of $|2,0\rangle$ and $|1,0\rangle$ states in the presence of a strong optical barrier as described in the main text. We then double the barrier's strength, inducing small amplitude sound waves traveling outward from the edges of the barrier. Fig. S2 shows the waves traveling outward on a spacetime diagram, from which we can then extract the speed of sound in this system. Our experimental measurements, corroborate the numerics and provide an estimate of the speed of sound of $v_s = 2.0(1)$ μm/ms. This result is consistent with the speed of sound determined by the analytical result in Eq. S11, at $v_s = 2.089$ μm/ms.

On the other hand, the branch obtained from ω_-^2 explicates that MI is present when $\omega_-^2 < 0$ for some range of values of the wavenumber k. This concurrently entails an exponential growth of the perturbations. Explicitly, this occurs when the constant term in the parenthesis of Eq. (S10a) is negative, i.e., $2(g_{11}Q_1^2 + g_{22}Q_2^2) < \mp\sqrt{\Delta}$, which in turn, immediately implies that MI takes place only for ω_-. Simple re-arrangements of the above conditions then show that a necessary and sufficient condition for the existence of MI is $g_{11}g_{22} - g_{12}g_{21} < 0$, namely that the mixture is immiscible. Notice that this result is consistent with the analysis of Ref. [4, 5]. In other words, even when all coupling terms are individually defocusing, MI still occurs if the cross-coupling terms dominate compared to the self-coupling ones.

When MI is present, further inspection of Eq. (S10a) determines the range of unstable wavenumbers, i.e., $|k| < k_{\max}$, with

$$k_{\max}^2 = 2\left(\sqrt{\Delta} - (g_{11}Q_1^2 + g_{22}Q_2^2)\right). \tag{S12}$$

It is straightforward to check that in the respective scalar reduction, the above expression agrees with established results. For instance, in the case of $Q_2 = 0$ and $g_{11} = 1$ (i.e., in the scalar defocusing scenario), one obtains $k_{\max} = 0$ (implying absence of MI), whereas if $Q_2 = 0$ but $g_{11} = -1$ (i.e., in the scalar focusing case), one recovers $k_{\max} = 2Q_1$ (e.g., see [7, 8]).

V. EXPANSION RATE OF THE MI WEDGE

Importantly, the linearized stability analysis presented above also allows one to obtain a prediction for the expansion rate of the MI wedge, as shown in Fig. 1 of the main text. Recall that, in a homogeneous one-component setting the propagation speed of the boundary of the DSW is the *minimum* of the linearized group velocity [7–9]. The same is true in our case. One can gain an intuitive understanding of this by considering how the various wave modes travel out from the narrow region of curvature near the central repulsive barrier. The sharp density gradient results in the excitation of a broad range of wavenumbers. Excitations corresponding to stable wavenumbers propagate away with the linearized group speed, and therefore do so with a speed larger than the minimum of the group speed. Therefore, the spatial extent of the DSW is confined to the region left over "behind", once the (stable) linear waves propagate away. Conversely, excitations corresponding to unstable wavenumbers grow without traveling producing the expanding DSW amplitude pattern.

In light of the above discussion, the edges of the modulated region are given by the minimum of the linearized group velocity associated with the branch $\omega_-(k)$ of the dispersion relation. In particular, from Eq. (S10a) we find the linearized group velocity

$c_g(k) = d\omega_-/dk$ as

$$c_g(k) = 2\frac{k^2 + g_{11}Q_1^2 + g_{22}Q_2^2 - \sqrt{\Delta}}{\sqrt{k^2 + 2(g_{11}Q_1^2 + g_{22}Q_2^2) - 2\sqrt{\Delta}}}, \tag{S13}$$

with Δ as in Eq. (S10b). The minimum of the above expression is found to occur when $k = k_{\min}$ with

$$k_{\min} = \sqrt{3}\sqrt{-g_{11}Q_1^2 - g_{22}Q_2^2 + \sqrt{\Delta}}. \tag{S14}$$

The corresponding minimum value of the linearized group velocity (S13) reads

$$c_{g,\min} = 4\sqrt{-g_{11}Q_1^2 - g_{22}Q_2^2 + \sqrt{\Delta}}. \tag{S15}$$

This yields Eq. 4 in the main text. As also discussed in the main text, Eq. (S15) reduces to the well-known prediction for the NLS equation in the scalar reduction. On the other hand, Eq. (S15) remains valid for arbitrary values of the ratio of the amplitudes of the two components. This result is a key outcome of our theory which can be readily compared against the direct numerical simulations, as well as the experimental observations, as is done in the main text.

Additionally, in the one-component setting, one can also describe the envelope confining the modulations of the nonlinear stage of MI. This was found in Ref. [6] to be

$$|q_\pm(m)| = q_0 \pm \frac{q_0}{m}\left[2 - m - 2(1-m)\frac{K(m)}{E(m)}\right], \tag{S16}$$

where m is the elliptic parameter and $K(m)$ and $E(m)$ are the complete elliptic integrals of the first and second kind, respectively [10]. The spatial mapping $m \mapsto x$ is given by $x/t = \sqrt{-g}\,\xi(m)$, with

$$\xi(m) = \frac{4q_0\sqrt{1-m}}{mE}\frac{(2-m)EK + E^2 - 3(1-m)K^2}{\sqrt{E^2 - (1-m)K^2}}. \tag{S17}$$

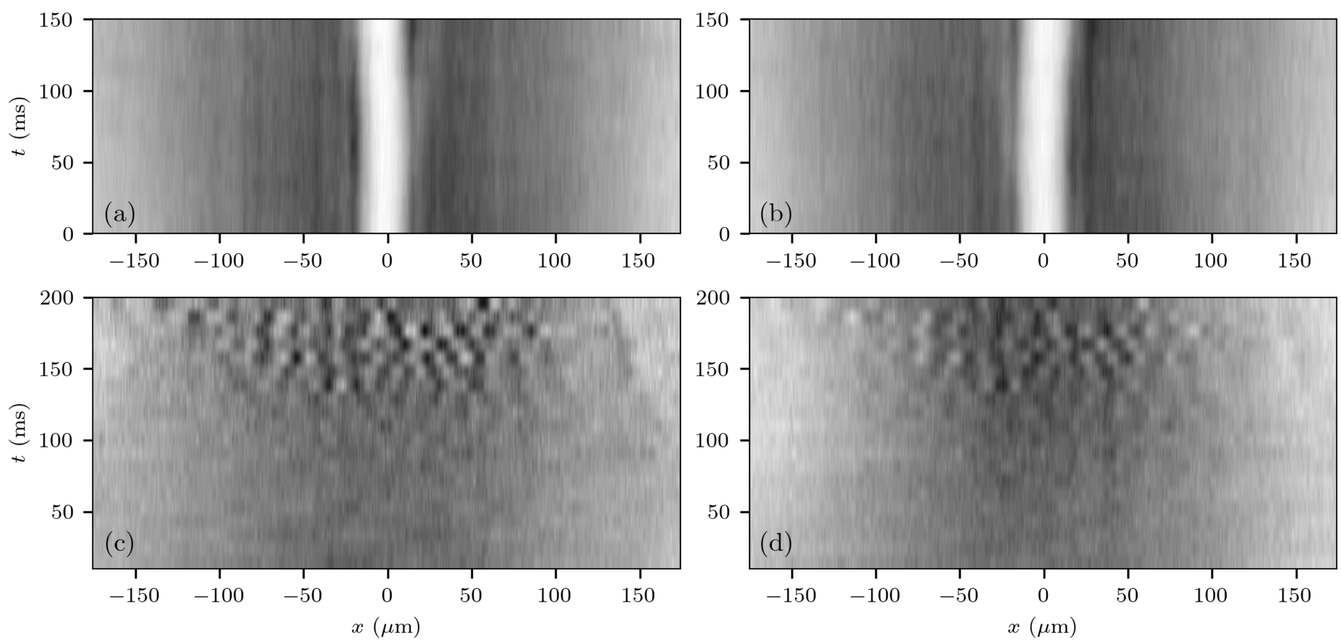

FIG. S3. Results for control experiments. (a)-(b) An equal mixture of the $|1,-1\rangle$ and the $|1,0\rangle$ states (shown in panels (a) and (b), respectively), is prepared in the presence of an optical barrier, using a similar experimental procedure to the one described in the main text. This specific mixture is miscible. Each row is an average over 11 experimental realizations for evolution times from 0 to 150 ms in steps of 15 ms. MI generation is absent in the miscible interaction regime. (c)-(d) An equal mixture of the $|2,0\rangle$ and the $|1,0\rangle$ states (shown in panels (c) and (d), respectively) is prepared without an optical barrier, using a similar experimental procedure to the one described in the main text. Each row is an average over 3 experimental realizations for evolution times from 0 to 200 ms in steps of 10 ms. Notice that MI sets in spontaneously after approximately 125 ms across the central bulk of the condensate. In all cases above, each spin distribution is independently normalized such that darker colors represent higher relative atomic density per pixel.

Taking the limit of $m \to 0^+$ in Eq. (S17) one can again obtain the speed $V_{\rm nls}$ [6, 8] described by Eq. (5) in the main text. Finally, as argued in the main text, Eq. (S16) adequately captures the MI wedge even in the weakly immiscible two-component repulsively interacting setting.

Incidentally, we point out that a DSW is a self-similar expanding structure, and as such it does not have a characteristic wavelength. Rather, its internal structure encompasses a range of length scales, as has been discussed in various review works, e.g., see [11].

VI. CONTROL CASES: IMMISCIBILITY AND THE BARRIER

To further elucidate the importance of the various parts of the experimental setup, we next look specifically at the key role played by two "ingredients": (i) immiscibility and (ii) the repulsive barrier. First, to clarify the role of immiscible interactions for MI nucleation, we experimentally reproduce the procedure described in the main text but now using a miscible mixture instead. For the miscible mixture utilized, the interaction parameters do not trigger the emergence of MI. Specifically, starting with all atoms in the $|1\rangle \equiv |1,-1\rangle$ state, we use a radio frequency pulse to prepare an equal mixture of the $|1\rangle \equiv |1,-1\rangle$ and the $|2\rangle \equiv |1,0\rangle$ states in the presence of the same optical barrier used in the main text. These hyperfine states are characterized by 3D s-wave scattering lengths $a_{11} = 100.4a_0$, $a_{22} = 100.86a_0$, and $a_{12} = a_{21} = 100.41a_0$, with a_0 denoting the Bohr radius. This is a miscible combination, as indicated by the fact that $a_{22} - a_{12}^2/a_{11} > 0$. Fig. S3(a)-(b) presents the density dynamics of the $|1,-1\rangle$ state and $|1,0\rangle$ state, respectively. It can be readily seen that, in sharp contrast to the magnetically insensitive states used in the main body of this work, this mixture is solely subject to small drifts due to minute residual magnetic gradients along the long axis of the BEC. As such, only trivial dynamics arise over the experimentally observed timescales, demonstrating the crucial role of immiscibility, and effectively attractive interactions, for MI generation. These dynamics have been independently verified using 3D GPE simulations following the experimental protocol. No MI was found even for longer timescales, which we have checked up to 500 ms.

Next, to illustrate the crucial role of the presence of the repulsive barrier, we consider the behavior of MI without the barrier, which more closely models a uniform mixture. Figure S3(c)-(d) shows an initially equal mixture of the $|2,0\rangle$ and the $|1,0\rangle$ states, respectively. We observe that without the barrier to catalyze MI, no significant dynamics occur until approximately 125 ms have passed. At this point spontaneous MI sets in across the bulk of the condensate, first near the center of the condensate where the density is highest, in agreement with the background behavior for the barrier induced MI demonstrated in the main text.

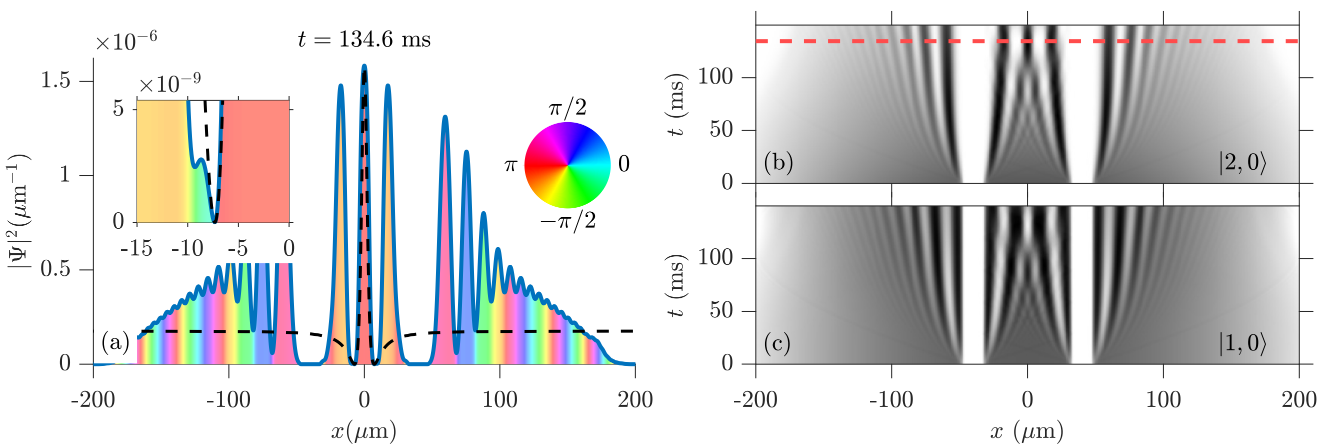

FIG. S4. 1D GPE simulations of the experimental procedure shown in Fig. 3. (a) Density profile of the $|2,0\rangle$ state at the instant at which a Peregrine-like structure forms around $x = 0$. In the inset, a magnification of the side dips is provided to clearly visualize the accompanied π-phase jump. The colormap denotes the phase at each spatial point. The dashed black line refers to the analytical Peregrine solution [Eq. (S18)]. (b)-(c) Spatiotemporal evolution of the $|2,0\rangle$ and $|1,0\rangle$ states, respectively in the presence of two repulsive potential wells. In panel (b), the red dotted line marks the time instant for the density profile shown in panel (a).

VII. DAM-BREAK PROBLEM AND THE PEREGRINE SOLITON

The Peregrine soliton is a solution of the focusing ($g < 0$) NLS [Eq. (S2)] with non-vanishing boundary conditions. In the context of the 1D GPE [Eq. (S3)] its equivalent solution has the form [12, 13]

$$P(x,t) = \sqrt{P_0}\left[1 - \frac{4\left(1 + 2i\frac{t-t_0}{T_P}\right)}{1 + 4\left(\frac{x-x_0}{L_P}\right)^2 + 4\left(\frac{t-t_0}{T_P}\right)^2}\right] e^{i\frac{t-t_0}{T_P}}, \tag{S18}$$

where $T_P\omega_\perp = L_P^2/a_\perp^2 = \hbar\omega_\perp/(|g|P_0)$. Here, T_P and L_P are the characteristic length and time scales of the Peregrine solution, respectively. Also, P_0 represents the background density of a homogeneous system, and g denotes the 1D single-component interaction strength.

In Fig. 3 of the main text, we discussed the experimentally monitored process of the interference of two dam-break problems emanating from the presence of two symmetrically placed repulsive potential wells and leading to the spontaneous generation of a Peregrine-like structure around the center. Figure S4 presents the corresponding dynamics obtained within 1D GPE numerical simulations emulating the aforementioned experimental procedure. The emergent spatiotemporal density evolution of the $|2,0\rangle$ and $|1,0\rangle$ states is depicted in Figs. S4(b) and S4(c), respectively. Note here the excellent agreement with the experimental results illustrated in Fig. 3 of the main text, where the generation of two counterpropagating DSWs triggered by the ensuing dam-break problems mimicked by the repulsive barriers is observed. Importantly, the interference of the DSWs within the region of the repulsive wells gives rise to the spontaneous nucleation of a Peregrine-like structure around $t_0 = 134.6$ ms [see the red dotted line in panel (b)], as can be deduced by comparing to the fit of the Peregrine analytical waveform [Eq. (S18)] demonstrated by the dashed black line in panel (a). In the inset of panel (a) we also provide a magnified version of the dips of the density visualizing the characteristic π-phase jump accompanying a Peregrine waveform (see color wheel).

It is important to keep in mind that in our setup we are dealing with a two-component particle balanced immiscible mixture. This lies away from the parametric regimes (high particle imbalance or attractive interactions) where a Peregrine soliton can be expected to be able to form, as it was the case of the experiment of Ref. [14]. Hence, in order to characterize the Peregrine-like structure shown in Fig. 3 and Fig. S4, we used the experimentally accessible values $P_0 = |\Psi_{|2,0\rangle}(x_0,t_0)|^2/9$ and $x_\pm = \pm 7.32$ μm, with $|\Psi_{|2,0\rangle}(x_\pm,t_0)|^2 = 0$.

[1] L. P. Pitaevskii and S. Stringari, *Bose-Einstein Condensation*, Oxford Science Publications No. 116 (Clarendon Press, Oxford, 2003).
[2] L. Salasnich, A. Parola, and L. Reatto, Physical Review A **65**, 043614 (2002).
[3] A. I. Nicolin and M. C. Raportaru, Physica A: Statistical Mechanics and its Applications **389**, 4663 (2010).
[4] P. Tommasini, E. J. V. de Passos, A. F. R. de Toledo Piza, M. S. Hussein, and E. Timmermans, Phys. Rev. A **67**, 023606 (2003).
[5] K. Kasamatsu and M. Tsubota, Phys. Rev. A **74**, 013617 (2006).
[6] G. Biondini, Phys. Rev. E **98**, 052220 (2018).
[7] G. El', A. Gurevich, V. Khodorovskiĭ, and A. Krylov, Physics Letters A **177**, 357 (1993).
[8] G. Biondini and D. Mantzavinos, Phys. Rev. Lett. **116**, 043902 (2016).
[9] G. Biondini, S. Li, D. Mantzavinos, and S. Trillo, SIAM Review **60**, 888 (2018).
[10] F. W. Olver, D. W. Lozier, D. W. Boisvert, and C. W. Clark, *NIST Handbook of Mathematical Functions* (2010).
[11] G. El and M. Hoefer, Phys. D **333**, 11 (2016).
[12] D. H. Peregrine, The ANZIAM Journal **25**, 16 (1983).
[13] A. Romero-Ros, G. C. Katsimiga, S. I. Mistakidis, B. Prinari, G. Biondini, P. Schmelcher, and P. G. Kevrekidis, Phys. Rev. A **105**, 053306 (2022).
[14] A. Romero-Ros, G. C. Katsimiga, S. I. Mistakidis, S. Mossman, G. Biondini, P. Schmelcher, P. Engels, and P. G. Kevrekidis, Phys. Rev. Lett. **132**, 033402 (2024).